



TECHNISCHE
UNIVERSITÄT
WIEN
Vienna University of Technology

DIPLOMARBEIT

Engineering dark states in hybrid quantum systems

*ausgeführt am Atominstitut der Technischen Universität Wien
unter der Anleitung von*

Univ. Prof. Dr. Hannes-Jörg Schmiedmayer

Univ. Ass. Dr. Johannes Majer

*eingereicht an der
Technischen Universität Wien
Fakultät für Physik
von*

Ralph Glattauer

Matrikelnummer: 0725762

Florianigasse 30-32/40 , 1080 Wien

Wien, am 26. Januar 2016

*It is often said that before you die your life passes before your eyes. It is in fact true.
It's called living.*

Terry Pratchett (1948-2015)

Abstract

Hybrid quantum systems combine physical systems with different properties to get the best of both worlds. In our case this means using nitrogen vacancy centers together with superconducting coplanar waveguide resonators. While the resulting system shows promising results, its usage is generally limited by decoherence effects.

In this thesis, we want to show a method to improve this by engineering long lived dark states that improve the decay dynamics of our system by a factor 10. This is significantly longer than the cavity or the spin decay, enabling our hybrid quantum system to perform better than its individual parts in this regard. We do this by actively shaping our inhomogeneously broadened spin distribution through the insertion of a high power signal at specific, freely chosen frequencies to excite these spins. The results in this thesis contributed to [\[Putz15\]](#).

We further test our system under strong driving fields and measure spin echos and bistability.

Contents

Abstract	iv
Contents	v
1 Cavity QED	1
1.1 Tavis-Cummings model	1
1.2 Inhomogeneous broadening and Cavity protection effect	4
1.3 Spectral hole burning	5
1.4 Spin decay	7
1.5 Bistability	9
2 NV^- centers	11
2.1 Level scheme	11
2.2 Spin Hamiltonian	12
2.3 NV ensembles	13
3 Superconducting Microwave Resonators	15
3.1 Coplanar Waveguide Resonators	15
3.1.1 EM field	16
3.1.2 Thermal occupation number	17
4 Dilution Refrigerator	19
5 Experimental setup	21
5.1 IQ mixing	22
5.2 Hardware setup	23
6 Measurements and Results	27
6.1 Testing the system	27
6.2 Avoided crossing	28
6.3 Rectangular probe signal	28
6.4 Giant spin oscillations	30
6.5 Hole burning	31
6.6 Hole burning spectrum	34
6.7 Hahn echos	37
6.8 Bistability	38

7 Conclusion and Outlook	41
A Frequency analysis of the holes	43
Acknowledgements	45
Bibliography	47

Chapter 1

Cavity QED

In the field of quantum optics, cavity QED describes the interaction of a light field in a cavity with atoms, particles or similar objects. The spin system used throughout this thesis are large ensembles of negatively charged nitrogen-vacancy centers in a diamond in conjunction with a superconducting coplanar waveguide resonator. Such systems function analogously to a cloud of atoms within an optical Fabry-Perot cavity and are described by the Tavis-Cummings Hamiltonian.

1.1 Tavis-Cummings model

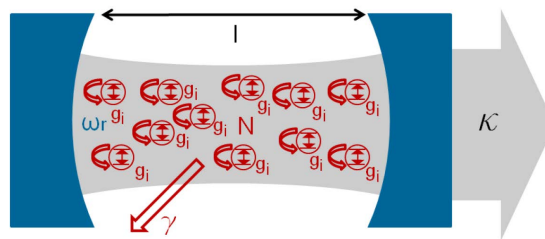


FIGURE 1.1: Simplified picture of our resonator-spin system, with N two-level systems, coupling g and loss channels κ and γ ([Kol12])

R.H.Dicke in 1953 was the first to analyze the coupling of a large number of two-level systems to a common field mode. In this case the emitters are able to interact with each other through their collective contact to the field, which means that we cannot treat them independently anymore.

The appropriate Hamiltonian for such a system, obtained by quantizing the field in the Dicke model, is the Tavis-Cummings Hamiltonian. It is the many particle version of the better known Jaynes-Cummings Hamiltonian ([TC68]), which describes only a single two-level system.

$$H = \hbar\omega_c a^\dagger a + \frac{\hbar}{2} \sum_j^N \omega_j \sigma_j^z + i\hbar \sum_j^N \left[g_j \sigma_j^- a^\dagger - g_j^* \sigma_j^+ a \right] - i\hbar \left[\eta(t) a^\dagger e^{-i\omega t} - \eta(t)^* a e^{i\omega t} \right] \quad (1.1)$$

The first term stands for the uncoupled resonator, the second term for the uncoupled spin ensemble, summing over the N two-level systems. The third term describes the interaction between these two and the fourth term represents the driving field with which we probe the cavity. The sum is required since all the spins have slightly different transition frequencies ω_j and coupling strengths g_j , which leads to inhomogeneous broadening (see below). ω_c denotes the cavities resonance frequency, σ_j^\pm , σ_j^z the individual Pauli spin operators, a^\dagger and a the creation and annihilation operators; and η stands for the driving field injected into the cavity.

We note that the fourth term cannot be found in [Dicke54] (but is necessary to describe our system), and that this picture does not include loss mechanisms.

The Dicke model describes the interaction of a large number of spins to a resonator. Out of N states from N spins, only one is a symmetrical and visible bright state, while the other $N - 1$ states are asymmetrical and nonradiant, therefore dark states ([Kur11]). For a better understanding we write these states for three spins connected to a cavity. The spin ground state is then given by

$$|0\rangle_s = |\downarrow\downarrow\downarrow\rangle \quad (1.2)$$

The symmetrical first excited state is

$$|1\rangle_s = \frac{1}{\sqrt{3}} (|\uparrow\downarrow\downarrow\rangle + |\downarrow\uparrow\downarrow\rangle + |\downarrow\downarrow\uparrow\rangle) \quad (1.3)$$

while all other possible excited states are asymmetrical. Coupled to the cavity, we obtain two polariton modes

$$|\pm\rangle = \frac{1}{\sqrt{2}} |0_c\rangle |1_s\rangle \pm |1_c\rangle |0_s\rangle \quad (1.4)$$

These modes are maximally entangled states between the cavity and the radiant spin state. Their position in the frequency spectrum is dependent on the collective coupling strength Ω of the participating spins. Loss mechanisms are introduced via the parameters κ and γ and combined in the total decay rate $\Gamma = \frac{\kappa + \gamma}{2}$. Γ is given by the HWHM of

the polariton mode peaks, while κ is given by the FWHM of the empty cavity resonance and describes the cavity decay via absorption or mirror losses.

This description holds in the strong coupling limit, where $\Omega > \Gamma > \kappa$. We reach this regime by collectively coupling to a large (10^{12}) number of spins, thus increasing the coupling strength by a factor of \sqrt{N} . A single spin couples to the cavity with ~ 10 Hz, leading to an effective coupling strength of $\Omega/2\pi = \sqrt{\sum_j^N g_j^2} \approx 10$ MHz.

If the number of excitations is much smaller than the number of spins, the Tavis-Cummings Hamiltonian can be reformulated and solved through a Holstein-Primakoff mapping([Ams13],[Hol39]). This approximates the large number of two-level systems as independent harmonic oscillators and allows us to change the spin operators to bosonic ladder operators:

$$\sigma_j^z = -\frac{1}{2} + b_j^\dagger b_j \quad (1.5)$$

$$\sigma_j^+ = b_j^\dagger \sqrt{1 - b_j^\dagger b_j} \quad (1.6)$$

This holds true for a small number of excitations ($\sigma_j^+ \approx b_j^+$), giving us the new Tavis-Cummings Hamiltonian

$$H_{TC} = \hbar\omega_c a^\dagger a + \hbar\omega_s b^\dagger b + \hbar\Omega (ab^\dagger + a^\dagger b) \quad (1.7)$$

with $b^\dagger = \frac{1}{g_{eff}} \sum_j^N g_j b_j^\dagger$

The eigenenergies then exhibit the avoided crossing mentioned above:

$$E_\pm = \hbar \frac{\omega_s + \omega_c}{2} \pm \frac{\hbar}{2} \sqrt{4\Omega^2 + \Delta^2} \quad (1.8)$$

with states

$$|+\rangle = \frac{1}{\sqrt{2}} (\cos \theta |1\rangle_s |0\rangle_c + \sin \theta |0\rangle_s |1\rangle_c) \quad (1.9)$$

$$|-\rangle = \frac{1}{\sqrt{2}} (\sin \theta |1\rangle_s |0\rangle_c - \cos \theta |0\rangle_s |1\rangle_c) \quad (1.10)$$

The decay parameters κ and γ are introduced via quantum Langevin equations for the photon and spin operators a and b , which also include the driving field η , which we insert into the cavity ([Ams13]). This leads to the Heisenberg equations of motion:

$$\dot{a} = -(\kappa + i * (\omega_c - \omega)) a(t) - i \cdot g_{eff} b + \eta \quad (1.11)$$

$$\dot{b} = -\left(\frac{\gamma}{2} + i(\omega_j - \omega)\right) b - i \cdot g_{eff} a \quad (1.12)$$

With this theoretical basis we can accurately model the transmission spectrum of our cavity.

1.2 Inhomogeneous broadening and Cavity protection effect

When interacting with a large ensemble of NV^- spins, we would like to imagine that all spins behave the same way, i.e. have the same transition energy. However, in reality only about 6% of the nitrogen in our diamond converts to NV^- centers ([Nob13]). This combined with other impurities and distortions in the lattice unpredictably influences each nitrogen vacancy. The excitation energies are no longer the same, but are distributed around the theoretical value and are given by a distribution function $\rho(\omega_s)$.

This is known as inhomogeneous broadening and not only makes it more difficult to address all NV^- spins at once, it also increases decoherence and is thus one of the main obstacles to overcome in hybrid quantum systems. Furthermore, the broadening changes the total decay rate Γ under the limit of strong coupling ($\Omega \rightarrow \infty$) to $\Gamma = (\kappa + \gamma + 2\pi\Omega^2\rho(\omega_s \pm \Omega)) / 2$ ([Diniz11]).

One way to reduce the total system decoherence Γ is the cavity protection effect. It occurs when the tails of the spectral spin distribution fall off faster than a Lorentzian lineshape. This is due to the Purcell effect ([Purc46]), which states that the environment affects the rate of spontaneous emission. Per Fermi's golden rule, an increased density of states leads to an increased transition (decay) rate. Conversely, when fewer decay channels are present because of the form of the spin distribution, decay is suppressed. This means increased decay with increased coupling while in the weak coupling regime, while causing the opposite effect in the strong coupling regime.

As shown in [Putz14], the exact form of our spin distribution $\rho(\omega)$ is that of a q-Gaussian with a linewidth of $\gamma_q/2\pi = 9.4$ MHz.

We can understand cavity protection as a reduction of loss channels to the spins in the polariton modes. These superradiant modes only occur under strong coupling and are themselves coupled to subradiant modes, which are their main source of decoherence. If the spin distribution falls off sufficiently fast these modes are energetically decoupled, strongly reducing decoherence. This is essentially the Purcell effect: reducing the number of ways these states can decay directly reduces the chance of decay itself.

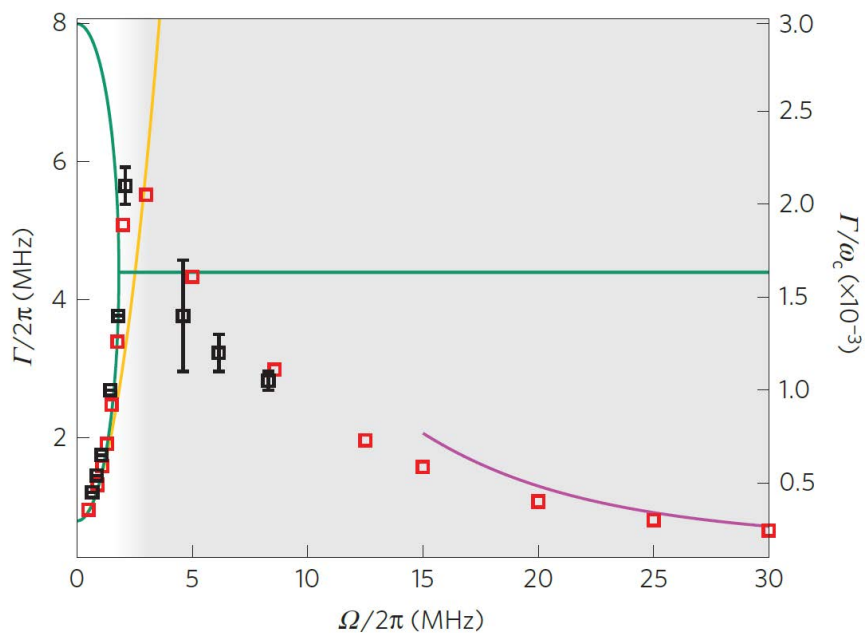


FIGURE 1.2: Decay dynamics dependent on coupling strength. Black: experimental results, Red: numerical results, ([Putz14])

1.3 Spectral hole burning

With this thesis, we want to show another way of dealing with the problem of inhomogeneous broadening by actively shaping the form of our spin distribution. This is possible through spectral hole burning: bleaching spins at certain frequencies (driving them into a mixture of excited and nonexcited states), effectively removing them from the system until they slowly decay back to their ground state.

To get a rough understanding of what is happening in our system when we do this, we turn to the aforementioned Dicke model. It describes how the states of our spin ensemble-resonator system hybridize into two polariton modes, visible as two peaks of our avoided crossing in the frequency spectrum. These two modes represent the two symmetrical bright states, while the other states are nonradiant. An excitation in this system oscillates between spin and cavity decaying at a rate given by the width (FWHM) of the peaks, which natively equals the total decoherence rate Γ .

When we remove spins out of this continuum at a specific frequency, the neighboring dark states interact with each other to bridge the created gap. The result is a temporarily visible dark state with a decay time according to its FWHM. We can think of this as superpositions of the states blue- (B) and red- (R) detuned from the hole. They can be written as an antisymmetric state

$$|A\rangle \approx \frac{1}{\sqrt{2}} (|\uparrow_B \downarrow_R\rangle - |\uparrow_R \downarrow_B\rangle) \quad (1.13)$$

coupled to the cavity state

$$|D\rangle \approx \frac{1}{\sqrt{\Delta^2 + 2g_\mu^2}} (g_\mu 2|0\rangle_c |A\rangle + \Delta|1\rangle_c |\downarrow_B \downarrow_R\rangle) \quad (1.14)$$

with detuning Δ and effective coupling strength g_μ ([Putz15]). These states are mostly antisymmetric and couple weakly to the cavity. This is illustrated in figure(1.3). Here, the resonator has its resonance frequency at 2.69 GHz and spin states hybridize to form an avoided crossing. Figure 1.3b shows the bridging of a hole in the middle of the state continuum, while 1.3c shows the states as we create them in the experiment.

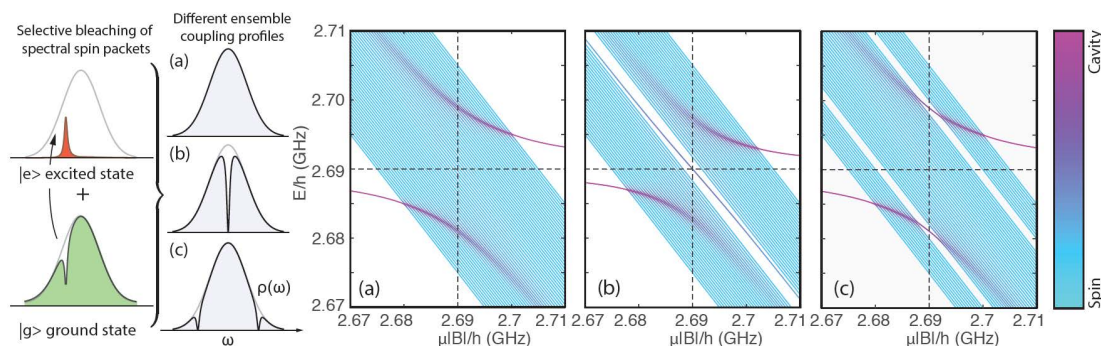


FIGURE 1.3: Spin distribution on the left, cavity/spin states on the right. The state continuum without holes(a), a hole in the middle(b), two symmetrical holes(c), color indicates whether states exist in the cavity or the spins([Putz15])

The exact shape of these new peaks is determined by the spectral width of the holes we create. It is this width that dominated the decay dynamics of excitations in the system when these engineered dark states are present. This new decay rate can be significantly lower than the previous total decay rate Γ .

The timeframe where this improvement holds is given by two timescales: Firstly the longer T_1 time with which the individual spins will decay back to their ground state. Secondly the timescale over which the created peak broadens and decreases in height due to interaction with spins of similar energy, given by the spin diffusion time. It is this

second, faster kind of decay that limits us in the experiment. Within this timeframe we may then perform additional measurements that exploit the improved properties of our system.

The frequency where we create these holes ideally lies slightly within the peaks of the avoided crossing ([Krim15]). Technically we can create the spectral holes at any point in the spin distribution, but the process works best and needs the least amount of input power at the points of highest transmission in the spectrum, i.e. on top of the polariton modes. However, since this process removes several percent of the available spin ensemble, the new Rabi splitting will be smaller than before and one should shape the peaks with this new form in mind.

This picture provides us with a rudimentary understanding of the dynamics of our system under the influence of spectral holes. For a more in-depth theoretical approach, we refer to [Krim15].

1.4 Spin decay

Working with spins always brings with it a host of unwanted processes that threaten to destroy coherence in a carefully prepared system. Thermal noise, interactions between spins of different energy and a number of impurities and lattice defects limit even the best experiments. While the literature tends to describe the following concepts mostly for nuclear spins, they also apply for the electronic nitrogen-vacancy spins in our diamond.

The two most important types of spin decay are spin-lattice decay and spin-spin decay ([Lev09]).

Spin-lattice relaxation or longitudinal relaxation is given by the time it takes the spins to decay from the excited state. Imagine a spin being polarized into the +1 state by a magnetic field. If we switch off the field, the longitudinal spin magnetization will decay according to

$$M_z^{el}(t) = M_{eq}^{el}(t) e^{-\frac{t-t_{off}}{T_1}} \quad (1.15)$$

where M_{eq}^{nuc} represents the equilibrium state and T_1 is the spin lattice relaxation time constant. This decay is temperature dependent and is caused by the spins interaction with its environment or spontaneous emission, and over time its state will decay towards its thermodynamic equilibrium.

Transversal or spin-spin relaxation describes the decay of the coherence between the many spins we find in our diamond. If polarized by a magnetic field they all show into this direction. Upon switching off the field, the spins then all start to decay. If all spins decayed at exactly the same rate, they would continue to show into the same direction, maintaining perfect coherence during the decay. However, due to interactions with the environment, the spin-spin alignment decays with the time constant T_2 until all spins show into random directions.

This decay of the transversal magnetization is described by

$$M_x^{el}(t) = -M_{eq}^{el} \sin(\omega_o)(t) e^{\frac{-t}{T_2}} \quad (1.16)$$

$$M_y^{el}(t) = -M_{eq}^{el} \cos(\omega_o)(t) e^{\frac{-t}{T_2}} \quad (1.17)$$

These kinds of decay can best be envisioned in the Bloch sphere, and the magnetization directions in these equations are labeled accordingly: the z-direction for the longitudinal relaxation and x- and y-direction for the transversal relaxation.

It is possible to remove the dephasing with a Hahn echo pulse sequence. This is done by sending in a $\frac{\pi}{2}$ pulse which rotates the spins into the x-y plane of the Bloch sphere where they loose coherence. After a time τ we send in a π pulse which rephases the spins. Once τ has passed again, we can measure a clear peak in the transmission since all spins are pointing in the same direction again.

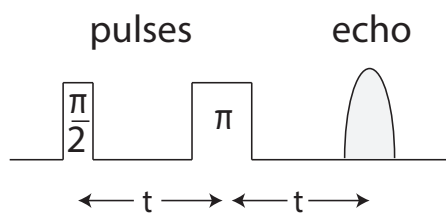


FIGURE 1.4: A Hahn echo sequence. The echo appears when the spins rephase.

There is another decay effect in our system called **spin diffusion**, which is created by the continuous exchange of energy with other spins. This causes decoherence since it changes the precession frequency of the spins unpredictably and irreversibly.

1.5 Bistability

While not the main focus of this thesis, we also measured another phenomenon our system can exhibit: bistability. Optical bistability occurs when a system can occupy two different states, dependent on how strongly it was driven previously ([Mart11]). In a plot of the input power versus the measured steady state output power this will show up as a hysteresis curve.

There are two reasons we are interested in this: Firstly, the ability to measure this effect depends on our magnetic field configuration. At [110] magnetic field direction (crystal frame), the resonator couples to only 2 of the 4 different NV^- subensembles. Using the [100] direction allows to couple to all 4 ensembles and increases the coupling by a factor of $\sqrt{2}$. Since the appearance of bistability depends on cooperativity, a parameter that depends quadratically on the resonator-spin coupling, we can increase it significantly this way. This makes the observation of bistability in our system highly dependent on the direction of the magnetic field.

Secondly, bistability is usually measured with optical resonators and atoms/spins that have very short excitation times. In contrast, our NV^- centers exhibit very large spin-lattice relaxation times with T_1 in the order of minutes. This means that the process wherein a constant probe signal drives our system into a steady state is macroscopically slow and directly observable. This is in stark contrast to the near instantaneous excitation times in optical experiments.

Bistability can be theoretically understood by looking at the Maxwell-Bloch equations. To make the calculation easier, we make a semiclassical approximation and assume that all expectation values of more than one operator can be factorized like $\langle \bar{a}^\dagger \bar{\sigma}_-^j \rangle \approx \langle \bar{a}^\dagger \rangle \langle \bar{\sigma}_-^j \rangle$. This neglects spin-spin interactions. We also use a driving frequency equal to the resonance frequency of our resonator, $\omega_d = \omega_r$. This then leads to the equations of motion for the photon and spin operators ([Mart11]):

$$\frac{da}{dt} = \eta - \kappa a + gN\sigma_- \quad (1.18)$$

$$\frac{d\sigma_-}{dt} = -(T_2^{-1} + i\Delta)\sigma_- + ga\sigma_z \quad (1.19)$$

$$\frac{d\sigma_z}{dt} = -\gamma(1 + \sigma_z) - 4g\text{Re}(a\sigma_-^*) \quad (1.20)$$

where Δ is the spin-cavity detuning. These equations are not solvable analytically. In order to derive bistability however, we only need to look at the steady state solution, setting the derivatives to zero. This gives us

$$\sigma_z = \frac{-1}{1 + \frac{|a|^2/n_0}{1+T_2^2} \Delta^2} \quad (1.21)$$

with the saturation photon number

$$n_0 = \frac{\gamma T_2^{-1}}{4g^2} \quad (1.22)$$

This ultimately leads to the mean photon number in the cavity:

$$|a|^2 = \frac{\eta^2}{\kappa^2} \frac{1 + T_2^2 \Delta^2}{(1 - C\sigma_z)^2 + T_2^2 \Delta^2} \quad (1.23)$$

The parameter $C = \frac{g^2}{\kappa\gamma}$ is the cooperativity and determines whether the system exhibits bistability. For lower values of the cooperativity we find no hysteresis and measure an almost linear increase in transmission when increasing the driving field. For higher values, the above equation results in three possible states for certain driving fields, as shown in figure 1.5. One of these solutions is unstable, giving us two possible states to measure, hence the name bistability. The state we end up in depends on the history of the system.

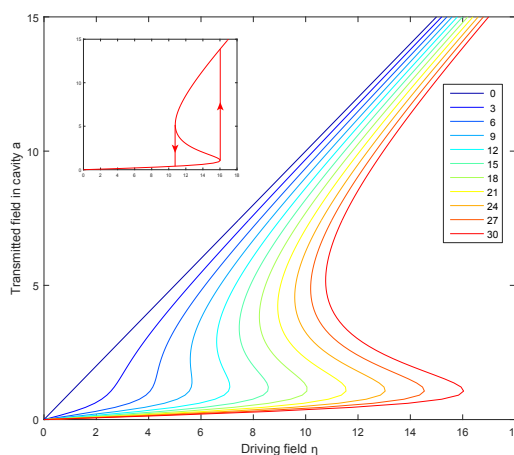


FIGURE 1.5: Cavity transmission depending on the driving field for different values of the cooperativity, for κ and n_0 set to 1 and zero detuning

Chapter 2

NV^- centers

For our experiment we require a great number of two-level systems coupled to our resonator. We choose NV^- centers in diamond for their high purity, low defect crystal, long coherence times, low microwave losses and transitions in the microwave regime.

A nitrogen vacancy center is a point defect in a diamond lattice ([Doh13]). Two carbon atoms are removed from the lattice, one is replaced with a nitrogen atom, the other remains a vacancy. The resulting NV^- center consists of 6 electrons: 3 come from the carbon atoms next to the vacancy, 2 from the nitrogen atom and 1 electron is taken from the lattice. It is this electron that makes the existence of the NV^- center possible, causing the resulting defect to carry a negative charge and giving it properties that make it very interesting for research.

The diamond used in this thesis is a HPHT (high pressure high temperature) crystal purchased from Element-6 containing nitrogen impurities. The vacancies were introduced into the lattice by neutron irradiation and subsequent annealing at 900 °C which supports the formation of the NV^- centers and helps heal out damage in the lattice.

2.1 Level scheme

The ground state of the NV^- features two unpaired electrons, making it a paramagnetic defect. It also exhibits a zero field splitting caused by spin-spin interaction, weakly dependent on strain and temperature. The ground state levels $0, \pm 1$ are subject to Zeeman splitting, allowing us to tune them into resonance with a cavity using a magnetic field (figure 2.2). It is further possible to excite the spins into the 3E excited state. This state preferentially nonradiatively decays into a 1A_1 singlet state through an intersystem crossing. It is possible to polarize nearly all spins in the ground state by exciting this

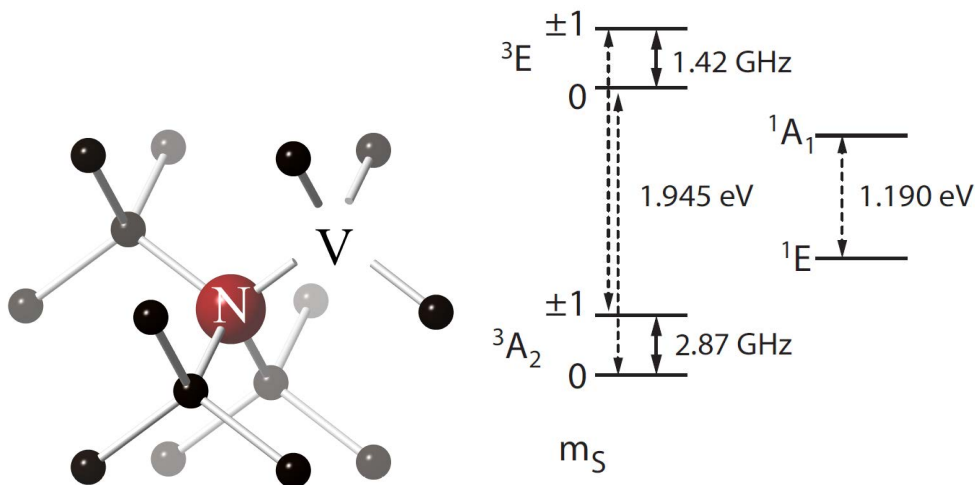


FIGURE 2.1: Left: Diamond lattice with nitrogen vacancy Right: NV^- level scheme ([Ams13][Kol12])

optical transition repeatedly. However, this is unnecessary at our working temperature of 25 mK, where over 99% of the spins are polarized into the ground state ([Ams13]). The experiments in this thesis are performed exclusively in this triplet ground state, specifically with the $m_s = 0$ and the $m_s = -1$ states, where an excited state exhibits a spin-lattice relaxation T_1 in the order of minutes at 25 mK ([Har06]). The optical transition to the excited state lies 1.945 eV higher and cannot be reached with the microwave signals we use.

2.2 Spin Hamiltonian

The corresponding spin Hamiltonian of a single NV is a combination of the zero field splitting Hamiltonian and the electronic Zeeman Hamiltonian and is given by

$$\frac{H_{spin}}{\hbar} = \begin{matrix} & |1\rangle & |0\rangle & |-1\rangle \\ \langle 1| & \left(D + g\beta_e B_z \right. & g\beta_e \frac{B_x - iB_y}{\sqrt{2}} & E \\ \langle 0| & \left. g\beta_e \frac{B_x + iB_y}{\sqrt{2}} \right. & 0 & g\beta_e \frac{B_x - iB_y}{\sqrt{2}} \\ \langle -1| & \left. E \right. & g\beta_e \frac{B_x + iB_y}{\sqrt{2}} & D - g\beta_e B_z \end{matrix} \quad (2.1)$$

The parameter D describes the deviation of the electron wave function from spherical symmetry, while E describes differences of its extension in the x - and y -direction, $\beta_e = \frac{\hbar|e|}{2m_e}$ is the Bohr magneton. The eigenequation of this Hamiltonian is most easily solved if the magnetic field runs parallel to the x , y or z direction, as is the case for our system (our field in z -direction is approximately zero). This causes the magnetic field dependency

to be quadratic for small fields and linear for large ones ($B \gg D, E$).

Furthermore, the Hamiltonian shows a significant level mixing due to lattice strain for low magnetic fields (1 mT). This is especially true for zero magnetic field, where the $m_s = +1$ and the $m_s = -1$ states are in a perfect mixture and m_s is no longer a good quantum number. Only at higher magnetic fields (>6 mT) these states are completely separated ([Ams13]).

2.3 NV ensembles

It is mainly their orientation to a magnetic field that differentiates spins in a lattice from free atoms in a conventional resonator. Within the diamond lattice, every vacancy is connected to 3 carbon and one nitrogen atom, thus 4 different NV^- configurations in the crystal are possible, each of them equally likely to exist. An arbitrary magnetic field applied to the system will split the energy levels of these subensembles, letting us couple to only one of them (This is limited in reality by the fact that we can only apply a very weak magnetic field in the z-direction to avoid creating vortices that disrupt our superconductivity). Aligning the field along one of the crystal axes results in affecting all 4 ensembles in the same way and allows us to couple to a maximum number of spins. In the experiment, the crystal frame is aligned as well as possible with the lab frame given by the magnetic field, with deviations of up to a few degrees possible. For our purposes we use a magnetic field at [110], where we affect only 2 ensembles. This requires less power than at [100] or [010], yet still allows us to easily reach the strong coupling regime. It also makes it easier to tune the magnetic field so that all used ensembles are in resonance. As visible in figure 2.2, the levels of the other two ensembles are significantly detuned from the resonator line and do not contribute to our measurements. This figure also shows us that for a magnetic field at [110], we need a total field strength of 87 mT to tune the NV transitions to match the resonator.

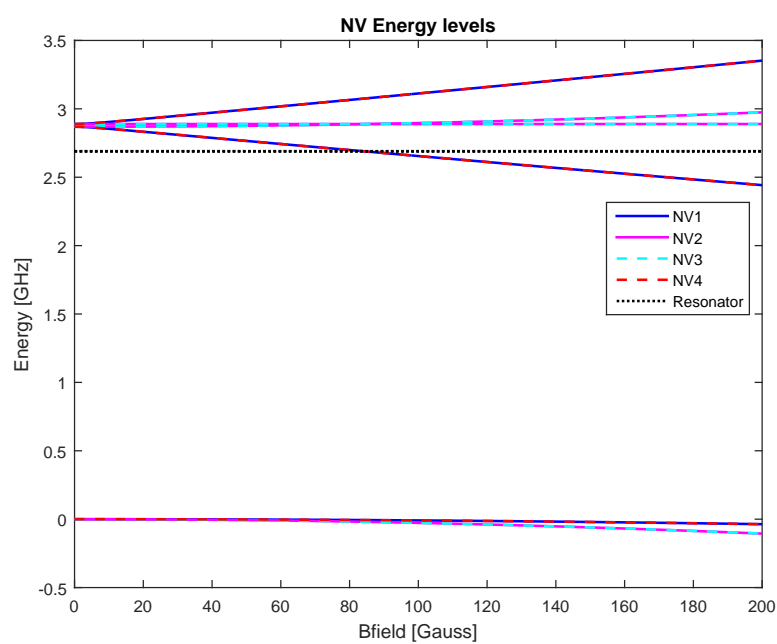


FIGURE 2.2: The energy levels in our system for the 4 NV ensembles at $[110]$ magnetic field. Resonator line in black

Chapter 3

Superconducting Microwave Resonators

Many quantum optics experiments look at the interaction of an atom- or spin-system with a localized light field. This is known as cavity QED. A standard application would be shining a laser onto a cloud of atoms within the confines of a resonator created by two high quality mirrors. Our experiment takes a different approach in that we use spins in a diamond crystal and create the necessary electromagnetic field with a superconducting resonator.

3.1 Coplanar Waveguide Resonators

The specific type of resonator we use is called a coplanar waveguide resonator. A CPW can be imagined as a flat coaxial cable: It has a central conductor surrounded by two ground conductors at both sides ([Ch97]). These conductors are composed of a flat superconducting metal, manufactured onto an insulating substrate. The waveguide is very long compared to its thickness and in our case designed as a triple pass configuration to allow increased overlap with the diamond that is placed on top of it. The impedance of a CPW depends only on the thickness of the center conductor and its distance to the ground conductors, making it easy to engineer a standard 50Ω of a coaxial cable. This keeps reflections due to impedance jumps at a minimum, since at both ends the CPW is connected capacitatively to a coaxial conductor. This allows us to probe our system via transmission measurements. Signals propagate in the CPW as transversal electromagnetic field modes between the center and ground conductors (see figure 3.2). The length of the resonator is necessarily set at half the wavelength of the desired resonance frequency, which in our case is given by $f_{res} = 2.897$ GHz and puts us firmly

into the microwave regime. Placing the NV^- -dotted diamond shifts this frequency to 2.69 GHz. The field along the CPW has the shape of half a sine period and is thus strongest in the middle where we place our diamond.

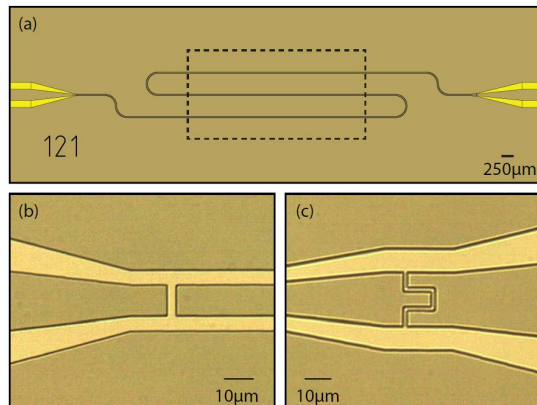


FIGURE 3.1: The resonator we used, conductor planes in brown and insulator in yellow. The diamond's position is indicated by dashed lines. b) and c) show the capacitive connectors we use to probe it, [Ams13]

As materials we use sapphire for the substrate and niobium films with a thickness of 200nm as the conductor. Niobium is superconducting below 9.2 K, greatly reducing losses and noise otherwise present in normal conductors. The waveguide is fabricated with standard optical lithography.

3.1.1 EM field

The electromagnetic vacuum field around the resonator can be estimated by integrating over the density of energy stored in the electric field([SG08]):

$$\frac{\hbar\omega}{4} = \frac{\epsilon_0}{2} \int E^2 dV = \frac{\epsilon_0}{2} E_0^2 V \quad (3.1)$$

This is half the energy of a field photon, the other half is in the magnetic field. These equations show that the amplitude of the electric field fluctuations is only dependent on constants and the mode volume of the resonator. While its length is fixed, its other dimensions can be designed to be very small due to its flatness. This is significantly smaller than in 3-dimensional cavities and strongly increases its vacuum Rabi frequency. In figure 3.2 we cut through the resonator to show the transverse electric and magnetic field. We note however that this picture assumes vacuum around the conductors, whereas in reality the permittivity of the dielectric material slightly deviates from ϵ_0 and slightly distorts the field lines. While we likened CPWs to a coaxial cables, their flat structure

means that the electromagnetic field is not confined through the outer ground planes, but decays quickly over distance from the center.

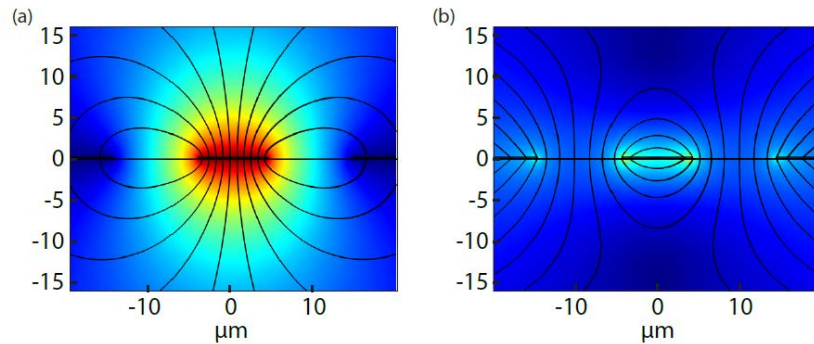


FIGURE 3.2: a) Electric field, b) Magnetic field in the resonator ([Ams13])

3.1.2 Thermal occupation number

The description of our system in the Tavis-Cummings model assumes the field in the resonator to be in the ground state, but since we cannot operate at a perfect temperature of 0 K, we must consider the thermal occupation number of our resonator. Any spins coupled to the resonator will, if left alone, reach an equilibrium state dependent on the mean photon number in the resonator, which is given by:

$$\bar{n}(\omega T) = \frac{e^{-\frac{\hbar\omega}{k_B T}}}{1 - e^{-\frac{\hbar\omega}{k_B T}}} \quad (3.2)$$

This formula shows that the thermal excitations in the resonator are only dependent on the temperature and the frequency. For our system (2.69 GHz and $T = 25$ mK), this means $\bar{n} = 0.0058$. Thus it is fair to assume that all spins are polarized to the ground state given the microwave frequencies we use. This is important for the validity of the Holstein-Primakoff approximation, as used in chapter 1

Chapter 4

Dilution Refrigerator

To polarize the spins into the ground state and reduce noise and thermal excitations, we operate our experiment at as low a temperature as possible. To accomplish this we use a dilution refrigerator by Oxford Instruments. It uses a $^3\text{He} - ^4\text{He}$ mixture to cool down to approximately 25 mK by exploiting the properties of these isotopes ([Lou74]). First, a precooling stage lowers the temperature in the fridge down to well below 1K through pulse tube refrigeration (works like a Sterling motor) and evaporative Helium cooling. This is helped by turbomolecular pumps that create a vacuum of as low as 10^{-6} bar in the fridge. At temperatures below approximately 870 mK, the helium mixture separates into two phases (see figure 4.1). One contains a normal $^3\text{He} - ^4\text{He}$ mixture, while the other phase is a dilution of superfluid ^4He and a certain amount of ^3He . These phases are separated by a phase boundary. With decreasing temperatures one phase will consist exclusively of ^3He , while all the ^4He concentrates in the other phase as a superfluid, containing only a small percentage of ^3He . The properties of this diluted phase are exploited to achieve the cooling effect. In particular, the fact that ^4He exists as a superfluid at these temperatures means that all ^4He atoms are in the same bosonic quantum state. This phase allows for a certain amount of ^3He within it, where every consecutive Helium atom added will have less binding energy than the previous one, similar to electrons in an atom. This allows for up to 6.6% ^3He in the diluted phase at low temperatures.

It is energetically advantageous for the diluted phase to contain this percentage of ^3He ; if we remove ^3He from it, the helium atoms from the pure phase will draw energy from the environment to make the phase transition until the ^4He phase is saturated again. Removing the ^3He is easy since the ^3He has a higher vapor pressure than the superfluid ^4He , so one can simply pump it off.

This principle results in a very efficient cooling of the system, potentially down to 2 mK, though our refrigerator is not quite this effective and 'only' reaches approximately 25 mK.

Once cooled down, we are usually able to operate our experiment at a near constant low temperature for over a month before having to warm up and start a new cooling cycle. There are several temperature stages within the cryostat separated by copper plates, and four cylindrical metal shields protect from thermal radiation. The outermost cylinder is visible in figure 4.2. Our experiment is mounted at the lowest and coldest stage of the setup within 3 pairs of Helmholtz coils.

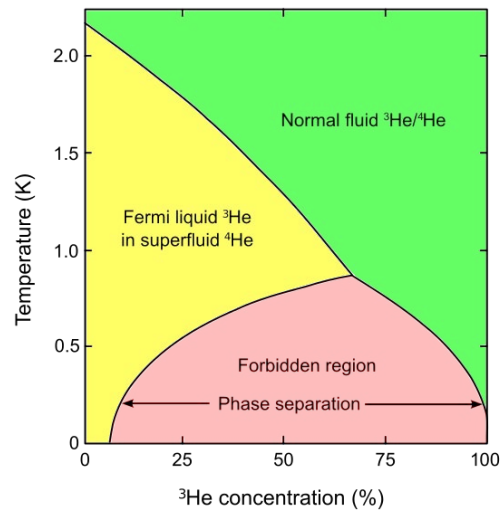


FIGURE 4.1: Phase diagram of a He3-He4 mixture, [Pob07]

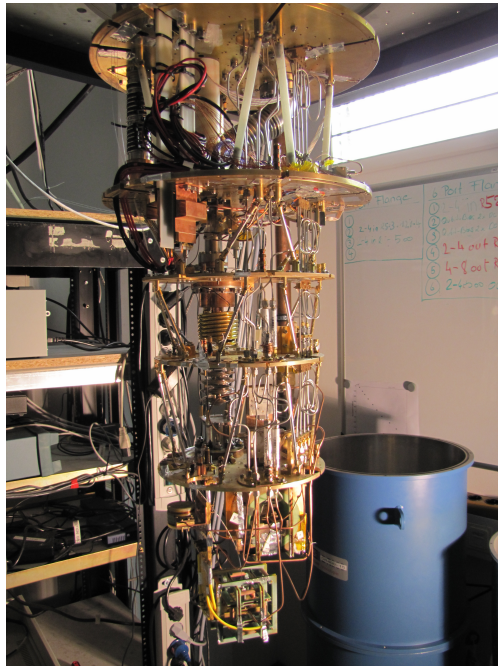


FIGURE 4.2: The open dilution refrigerator. To the right: Blue metal hull that covers the fridge when it is closed

Chapter 5

Experimental setup

As stated above, all measurements are performed within the dilution refrigerator at a temperature of 25 mK. We use 3 Helmholtz coils to apply magnetic fields up to 16 mT. The diamond sample we use carries a large number of NV^- Centers, of which about 10^{12} can couple to the resonator. A single vacancy couples with a strength of $\frac{g_0}{2\pi} \approx 12$ Hz. The system we probe is this diamond crystal fixed to a CPW resonator. This setup is mounted in a copper box to limit the noise background to certain well-defined frequencies and shield from thermal radiation. Its Quality factor of $Q=3100$ is significantly lower than that of the bare cavity because the diamond acts as an additional loss channel.

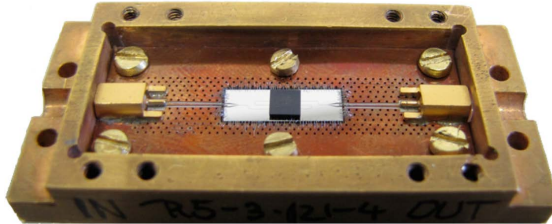


FIGURE 5.1: Resonator with diamond

With this system, many basic measurements can be performed by using a vector network analyzer (VNA), which probes the system with a given power at varying frequencies. This is the easiest way to measure a spectrum and thus determine the parameters of the resonator like resonance frequency or decay constants. Unfortunately, this method is relatively slow and unable to capture the interesting dynamics our system exhibits at the micro- or nanosecond level. To accomplish this, we use IQ mixing.

5.1 IQ mixing

IQ mixing, or Quadrature Amplitude Modulation (QAM) is a signal transmission technique common in modern technology like cellphones or television. Two signals consisting of an I_{in} (in phase signal) and a Q_{in} (quadrature signal) component are mixed onto a carrier frequency (selected to be our systems resonance frequency) also known as the local oscillator (LO). There is a 90° phase deviation between the two components. The mixed signal is transmitted and then mixed down again. We then analyse the measured I_{out} and Q_{out} components, allowing us to obtain the complete signal given by an imaginary function. One can visualize this by looking at the $e^{i\phi}$ function in imaginary space: it takes the form of a spiral. Its sine and cosine parts can then be extracted by projecting that spiral onto a plane. A standard measurement will only capture one of these components. Only by measuring and combining both (with a 90° phase difference between them), we can reconstruct the whole signal.

The signal sent into the resonator is then given by:

$$A = I_{in}(t) \cdot \cos(\omega t) + i \cdot Q_{in}(t) \cdot \sin(\omega t) \quad (5.1)$$

To extract the I and Q components from the mixed signal, it is demodulated through a mixer with the same carrier signal (homodyne detection scheme). This way we obtain I_{out} and Q_{out} , and can then calculate the amplitude $A = \sqrt{I_{out}^2 + Q_{out}^2}$ and the phase difference between the two components $\phi = \arctan\left(\frac{I_{out}}{Q_{out}}\right)$.

It is instructive to view a measurement in the I/Q space. To do this we measure the cavity response of our system by sending in a constant signal. This drives the system into a steady state, from where it decays after we switch off the pulse. Figure 5.2 shows this in I/Q space. The length of the excitation marks the amplitude, its angle gives the phase ϕ . The resonance frequency can also be determined with such a measurement, since an off-resonant signal produces a curved response. Furthermore, changing the ratio between I and Q while keeping A constant will only change the phase and doesn't affect the system's response in our experiment.

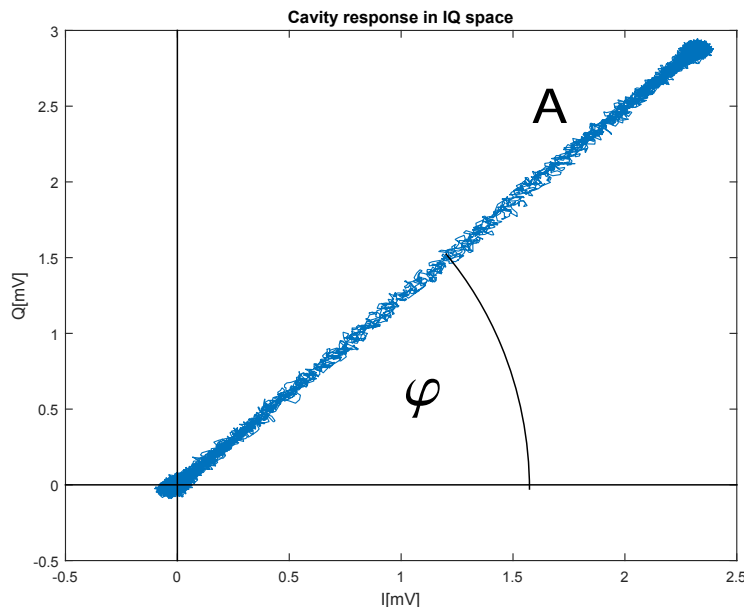


FIGURE 5.2: Cavity response in I/Q space

5.2 Hardware setup

In our first attempts to create spectral holes we generated symmetric frequency peaks by sending a sine wave into the mixer. A Fourier transform shows that mixed onto the carrier this creates a signal with two symmetric peaks around the carrier frequency, whose distance is determined by the frequency of the sine. While it is possible to perform our experiments in this way, over time it became apparent that for the holeburning measurements we wanted to attempt, we needed to create sharper, better peaks in the frequency spectrum than our previous setup allowed.

An improved way to burn the holes is to use additional frequency generators as local oscillators to create the holes directly.

This also has the advantage of allowing us to influence the shape of the spectral holes with our I and Q input. This shape is specifically determined by the Fourier transform of the I/Q input. For example, an exponential signal creates a Lorentzian frequency profile, while a Gaussian signal creates a Gaussian profile (a Fourier transformed Gauss distribution is a Gauss distribution).

This is done by combining the two carrier frequencies we use for the hole burning process to create the LO of one mixer, whose I/Q input is a function that determines the shape of the holes. Shortly after, a second mixer with an LO at resonance transmits a probe signal. We shift between these measurement methods very quickly by using a

nanosecond switch.

One of the advantages of using IQ mixing is that it allows us to interact with the resonator within very short timeframes. This is determined by the resolution of the arbitrary waveform generator (AWG) we use to create the I and Q components, and is in our case limited to 0.5 ns. Meanwhile, measurement readout is performed with a 5Gs oscilloscope. The carrier frequency these signals are mixed onto lies at 2.69 GHz, driving the $|0\rangle$ to $|-1\rangle$ transition.

The signal we generate this way is sent via coaxial cables into the dilution refrigerator and to the resonator, which is coupled capacitatively and sits in a copper box in the middle of the 3 Helmholtz coils (see figure 5.3).

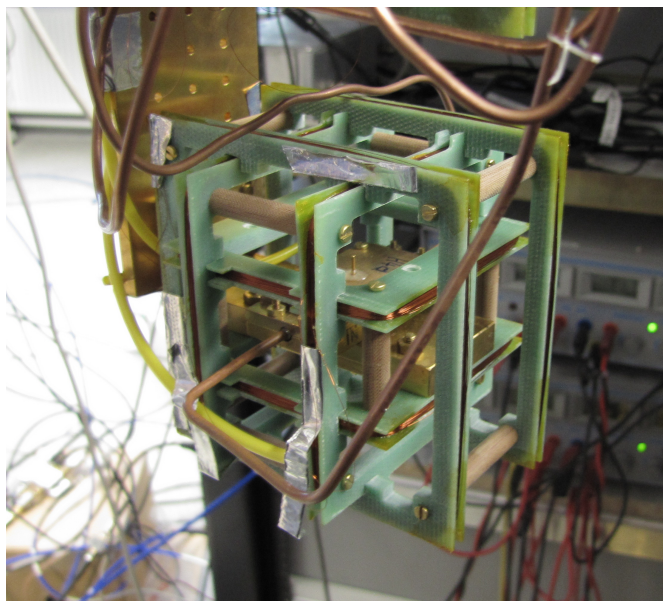


FIGURE 5.3: Helmholtz coil setup, resonator casing in the middle

Previous experiments in our dilution refrigerator were performed with very low driving powers and needed $10^5 - 10^6$ averaged measurements in order to sufficiently cancel out noise (see for example [Putz14]). Our old setup also included several strong attenuators in the dilution refrigerator, reducing the drive signal's strength by 60 dB before it entered the resonator.

In these new experiments we aim to bleach several percent of the available spins in our system, requiring far more power than previously. To achieve this, we removed the attenuators and installed additional amplifiers in order to increase our total input power by over 10 orders of magnitude, allowing us to perform single shot measurements.

However, being able to input high power signals into our resonator comes with a drawback: Special care must be taken to make sure the system is only probed for a short

amount of time during the measurement. Sending in a signal (even amplified noise) for longer than a few milliseconds may significantly heat up the resonator and the fridge, necessitating a longer cooldown period. We avoid this by using a switch to completely shut off the signal within a few nanoseconds.

For better remote control over the measurement power we also use digital attenuators and a second switch that can route the signal through a high power amplifier. A third switch connected to another mixer and two microwave signal generators allows us to create clear frequency peaks at two different frequencies and then perform a homodyne measurement at resonance frequency.

A simplified circuit diagram of the setup is shown in 5.4.

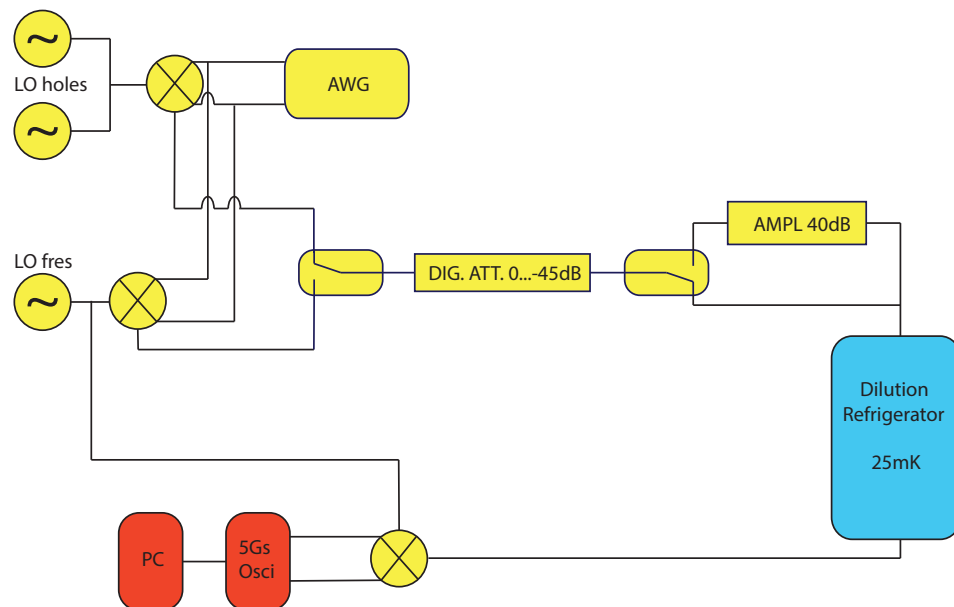


FIGURE 5.4: Our measurement setup. Not shown: additional amplifiers, attenuators and noise filters, LO leakage correction for IQ mixing

Chapter 6

Measurements and Results

After discussing the theoretical background of what we attempt to achieve and showing our experimental setup, we now discuss the specific measurements and their results that were performed in the course of this thesis. We demonstrate the significant improvements possible through spectral holeburning and its effect on the polariton modes. We show the possibility of spin echo measurements with our spin ensemble. Finally, we measure bistability on extremely long timescales ($>10000s$). In order to reduce the noise contribution most measurements are averaged up to 100 times.

6.1 Testing the system

The work horse of our experiments is the coplanar waveguide resonator R121 coupled to a diamond containing a large amount of NV^- centers.

The resonance frequency of the resonator changes from the theoretical 2.87 GHz (chosen to be close to the NV^- transition) due to dielectric loading when the diamond is placed upon it. This also changes the Quality factor Q from ~ 15000 to ~ 3100 .

Without a constant magnetic field the resonator shows a single peak at $f_{res} = 2.69$ GHz, while the NV^- transition to the ± 1 level lies at 2.87 GHz. At this point the resonator is far detuned from the NV^- levels and will act almost like an empty cavity. We can probe this system with a constant signal to measure the cavity response and by fitting of the exponential decay we obtain the cavity decay rate $\kappa/2\pi = 0.838$ MHz(FWHM).

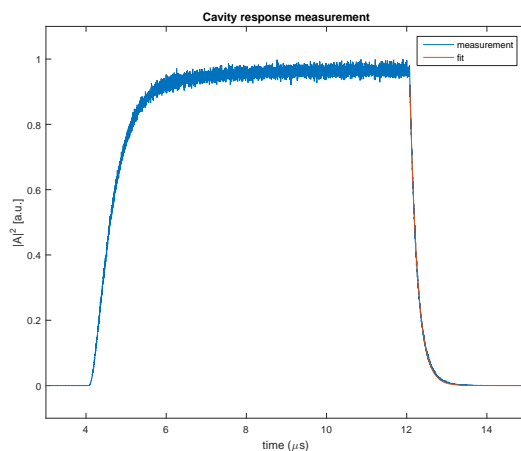


FIGURE 6.1: the cavity response of our system, far detuned from resonance

6.2 Avoided crossing

The resonator- NV^- system must be tuned into resonance for our experiments. This is done by increasing the magnetic field in the $[110]$ direction until we can observe the avoided crossing. The system works best when both peaks are the same height, then a signal sent in at resonance interacts with both peaks equally. However, this is complicated by the existence of a Fano resonance. This resonance stems from the interference of two scattering amplitudes: the scattering within the continuous background noise and the scattering of the discrete resonance of the resonator. It is clearly visible to the left in figure 6.2 as the difference in amplitude above and below the avoided crossing. We correct for this by subtracting the effect and tuning the magnetic field so that the height of the left peak in our avoided crossing is smaller than that of the right one. This allows for the best interaction between the spins and the cavity and gives us our ideal polariton modes (to the right in figure 6.2). From this we obtain the resonator-spin coupling $g = 10.4$ MHz, measured as half the distance between the two peaks. The fact that we measure this avoided crossing proves that we have reached the strong coupling regime.

6.3 Rectangular probe signal

To test our system we perform a simple measurement: We send a constant pulse with a length of 800ns into the resonator until the system is driven into a steady state, then switch off the signal. This allows us to observe Rabi oscillations ([Rabi37]), which occur in a two-level system under the presence of a light field with frequency close to resonance. Under these conditions the state in the system will oscillate between the two

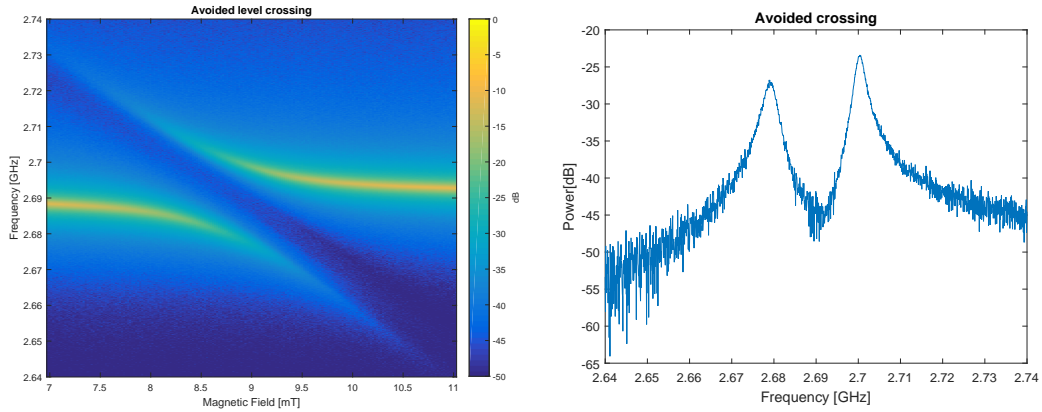


FIGURE 6.2: the avoided level crossing of our resonator

levels. Due to the validity of the Holstein-Primakoff approximation, this also happens in our experiment, where the energy will oscillate between the resonator and the spins. The signal shows a pronounced overshoot after the drive is switched off, visible even in the second oscillation peak (figure 6.3). These damped Rabi oscillations have a frequency corresponding to the Rabi-splitting of the polariton modes and decay with the total decay rate Γ .

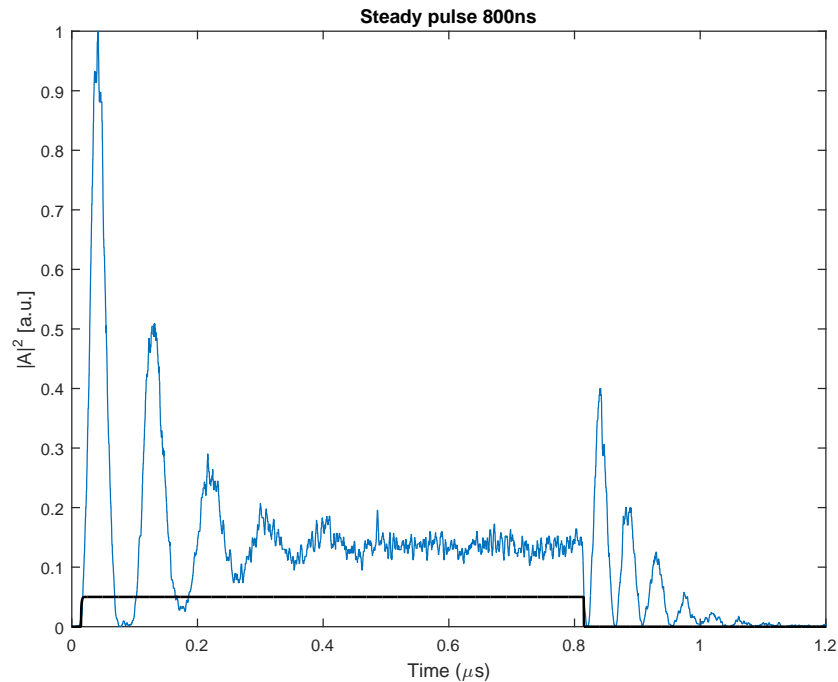


FIGURE 6.3: A steady pulse measurement with transmitted signal (blue) and probe pulse (black), showing Rabi oscillations and a strong overshoot

6.4 Giant spin oscillations

We can further test our system and excite giant spin oscillations by sending in a sinusoidal signal. Like a pendulum stimulated at its resonance frequency (in our case the frequency corresponding to the Rabi splitting), this drives the spins until a maximum oscillation amplitude is reached, after which we switch off our drive. The spins then dephase and thus lose coherence with a decay rate of $\Gamma/2\pi \approx 3$ MHz (FWHM).

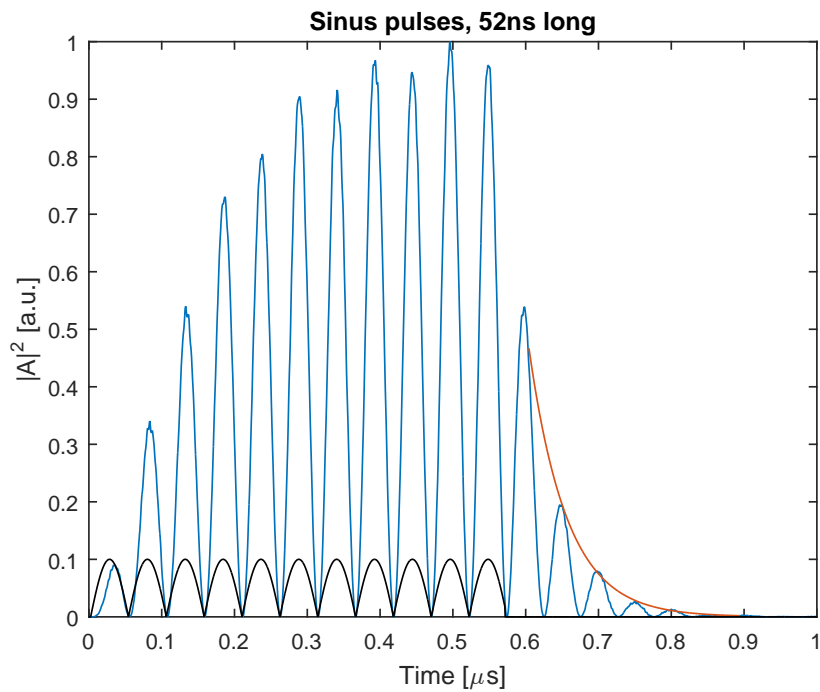


FIGURE 6.4: Excited sinus oscillations in our cavity with signal sent in (black), transmission (blue) and fitted decay (red)

6.5 Hole burning

Until now, all measurements were done within the confines of the weak driving limit. This means that the number of spins we excite at a certain energy E_s is much smaller than the total number of available spins at that energy.

We now want to see whether we can improve these decay times/coherence rates. To accomplish this, we increase our driving power until we reach the strong driving regime. Repeating the same measurement as above then alters the shape of the spin distribution for a relatively long time (about $100\ \mu\text{s}$), since a significant number of spins is now bleached. This way we selectively alter our spin ensemble at specific positions, i.e. hole burning.

We achieved the first positive results by mixing a sine signal with a frequency corresponding to the desired hole position onto the carrier wave. However, this has the disadvantage of creating somewhat unclear frequency peaks, mainly due to slight errors in the mixing setup. Thus we changed our setup so we could burn the holes with frequency generators (see chapter 5.2). This also allows fine control over the shape of the frequency profile, and after many tries we achieved the best results in terms of coherence times with a Gaussian envelope switched off at its maximum, which allows us to best examine its decay. This creates a Gauss-like frequency profile with a FWHM of 473 kHz (for the exact shape see Appendix A).

When burning these holes, we want to create them with a very narrow width, since a small FWHM leads to longer decay times. On the other hand, thin holes smear out due to spin diffusion (see below) much faster than thicker ones. To optimize the parameters, we also vary certain parameters in our experiment: the power, the frequency at which the holes are burned (determined by the wavelength of the sine wave) and the spectral width of the hole. Such a measurement is shown in figure 6.5, where we slowly increase the power of the hole burning signal. Once a threshold is reached at about $-20\ \text{dBm}$, the system decoherence rate is strongly reduced. We also vary the carrier frequency in another measurement visible in figure 6.6, where we find that the excited oscillations are the most pronounced very close to resonance. A slightly off-resonant signal will create I and Q components which are out of phase and thus reduce contrast this in the amplitude A.

We also performed these measurements in the $[100]$ magnetic field direction, with no significant difference in the results (expect for needing about 3 dB more power since the number of spins coupling to the resonator doubled).

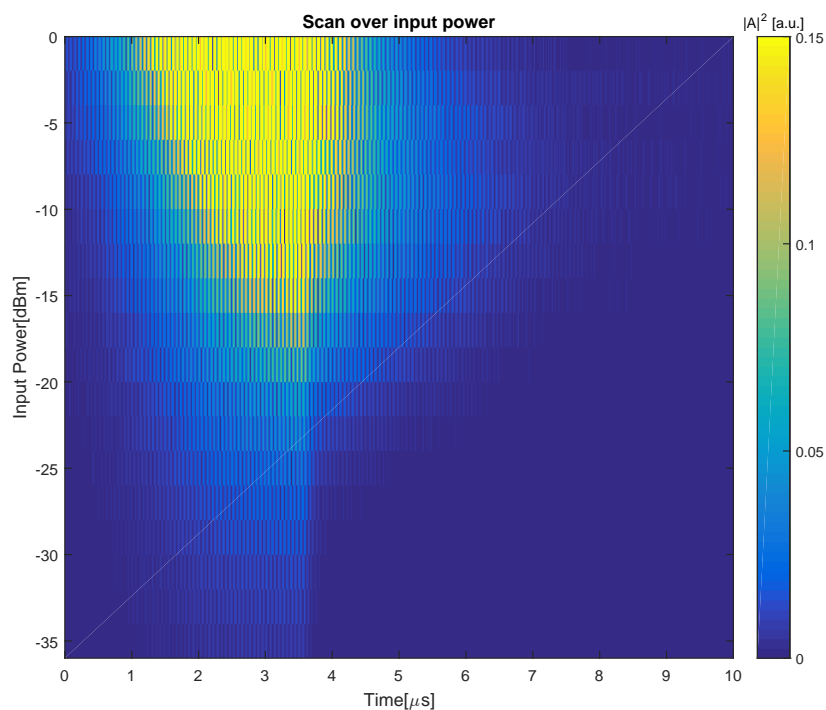


FIGURE 6.5: Increasing power sent into the fridge when burning spectral holes, minimum decay rate at ideal power

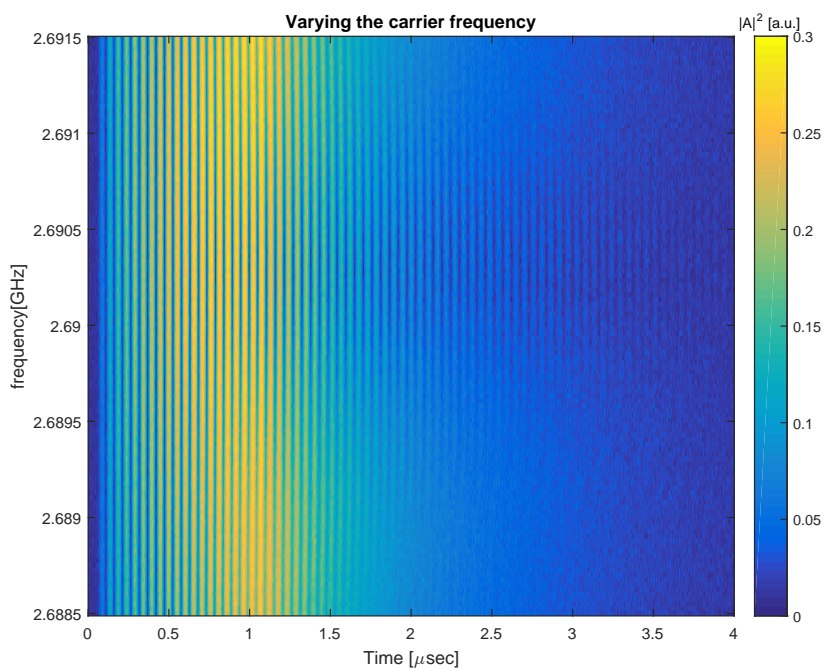


FIGURE 6.6: An off-resonant carrier frequency causes the I and Q parts of the measured signals to be phase shifted with respect to each other. This is visible in the oscillations of the amplitude A when we vary the carrier frequency.

The results of our efforts are visible in figure 6.7: we excited giant spin oscillations with and without spectral holes in our spin distribution by sending in 15 sine pulses. The effect is an improvement in the measured decay time of our spin ensemble. We also observe a higher transmission with the burned hole, so that the excited oscillations reach a higher amplitude than before (also visible in the spectrum below). Another interesting feature visible here is the existence of two kinds of exponential decays when the holes are present. For the normal, untouched oscillations we measure the expected decay of $\Gamma/2\pi = 2.91$ MHz, which corresponds to the total decoherence rate in our system. On the other hand, for the oscillations after we burn the hole we first observe a quick decay rate of $\Gamma'/2\pi = 1.11$ MHz and then a slower decay at $\Gamma_{hole}/2\pi = 419$ kHz. First, the faster decay rate Γ' corresponds to the width of the polaritonic peaks, modified by the hole burning and interference between the energy stored in the spins and the resonator ([Putz15]). This is followed by the slower decay rate Γ_{hole} , which is dominated by the created dark states.

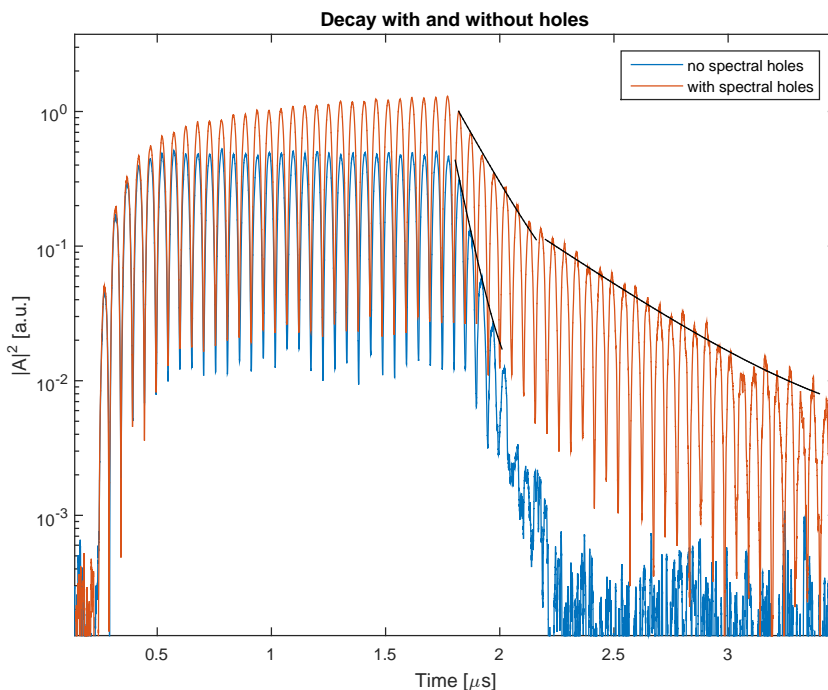


FIGURE 6.7: Excited oscillations and state decay with (red) and without (blue) previously burned holes and fitted decay (black)

While we see a significant improvement in coherence time in 6.7, it does not show the limit of what is achievable with our setup. The pulse sequence used to demonstrate the effectiveness of our scheme was sent in $8.5 \mu\text{s}$ after the holeburning pulse. This wait time is necessary to allow the excitations from the holeburning sequence to leave the cavity. However, since the improvement only lasts for a limited amount of time and deteriorates afterwards (see below, figure 6.10), the best possible decay time is measured

in the decay of the hole burning pulse itself. We show this in figure 6.8, where the plotted line is taylorred to the decay at $\Gamma_{hole}/2\pi = 245$ kHz. This result is remarkable since it shows an improvement of the decay rate by more than a factor of 10, making Γ_{hole} even smaller than the cavity decay rate κ . Extensive testing has not yet produced a result significantly better than this, suggesting that this is the limit for our setup.

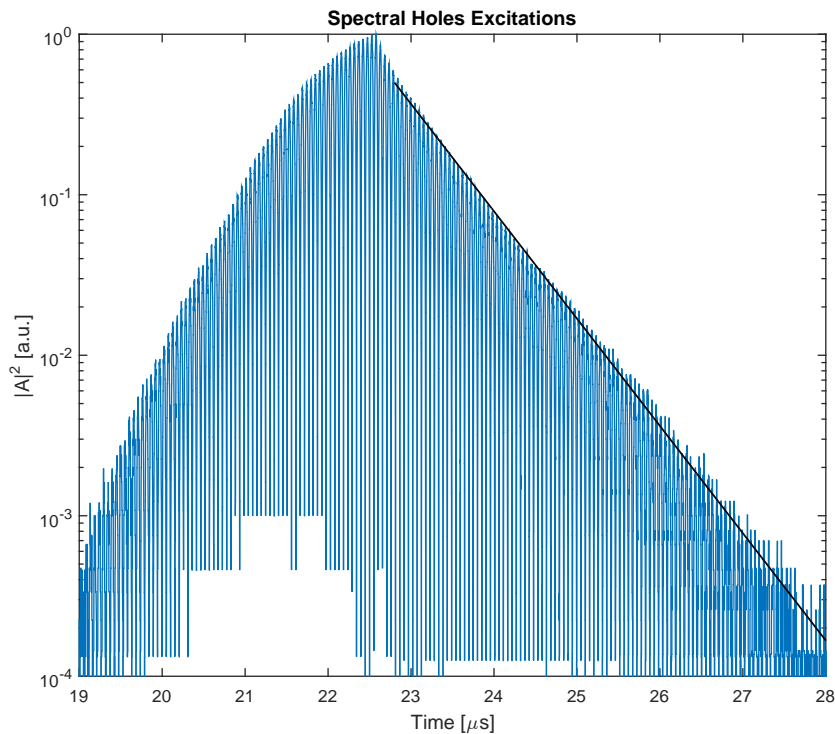


FIGURE 6.8: Decay of the excitations created by the holeburning pulse itself

6.6 Hole burning spectrum

Since we significantly changed our spin distribution, we are now interested in the new shape of our avoided crossing right after the hole burning process. While previous measurements of the avoided crossing were performed with a vector network analyzer (VNA) that probed the system for a short amount of time while sweeping through the desired frequency range, the short lifetime of the holes makes it necessary to use our IQ mixing setup. Here we essentially do the same thing the VNA did, but on a much smaller timescale: After burning the holes, we use a rectangular pulse with a length of several microseconds to probe the system. Another such pulse is sent in before the holeburning signal for comparison. We then take the mean of the steady states that the two pulses reach. By varying the carrier frequency of the rectangular pulses, we can slowly reconstruct the whole avoided crossing. The main disadvantage of this process

is that it takes much longer than a spectrum taken with the VNA, mainly due to the longer waittime between each successive measurement. Nevertheless, this is necessary to make sure that almost all spins have once again reached the ground state.

The result is visible in figure 6.9. Comparing the two plots shows that the holeburning process shapes a new avoided crossing that is more pronounced than the old one. This effect is almost completely limited to the two polariton modes. The higher and sharper peaks mean a greatly reduced decay rate. The new effective coupling strength g_{eff} is given by the new positions of the peaks and is slightly reduced due to the removal of spins from the ensemble.

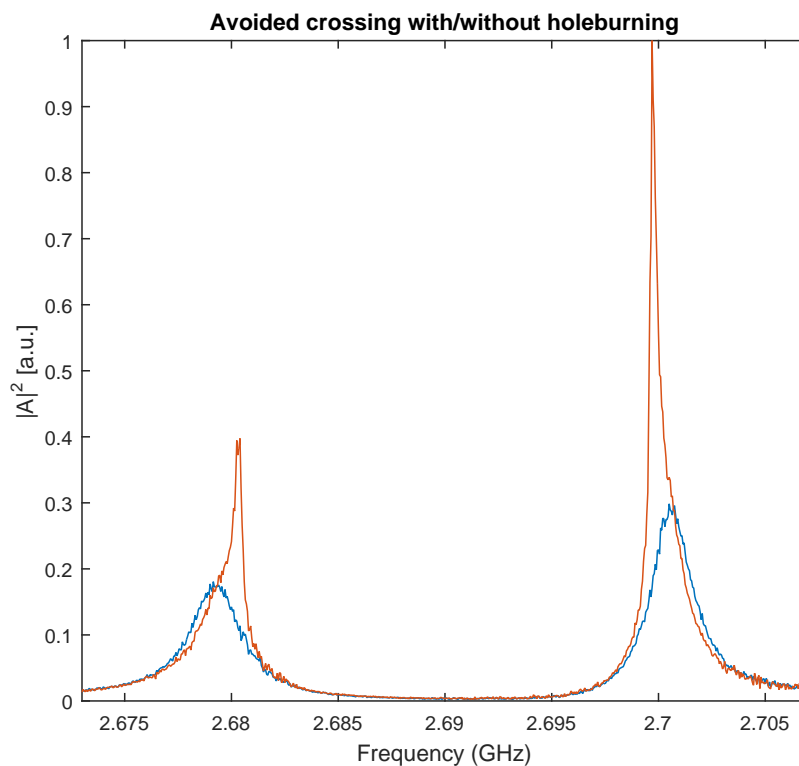


FIGURE 6.9: The avoided crossing with and without holes, measured by IQ mixing. Old avoided crossing in blue (without holes), new one in red (with holes)

We note that this new avoided crossing will slowly change back to its previous shape. There are two decay processes involved in this: The spin-lattice decay T_1 and the spin diffusion time T_1^* . The decay time T_1 is responsible for the slow decay of the spins we raised into the excited state. The effect on the avoided crossing is relatively small: by burning the holes we excited a small amount of spins in the system, thus decreasing the coupling strength g_{eff} . This moves our peaks slightly together and it will take a few minutes until all spins are once again in the ground state. The spin diffusion mechanism

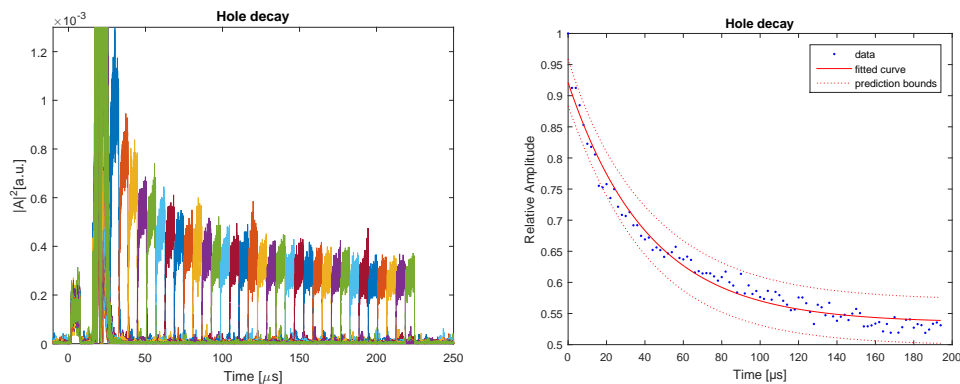


FIGURE 6.10: Measuring the decay of the spectral holes. Probe pulses with increasing wait-time (left) and fitted decay (right)

works on a much shorter timescale and is responsible for the decay of the peaks that we created on top of the normal polariton modes in our spectrum.

To measure this decay, we perform an experiment similar to the previous one: We first send in a rectangular control pulse for reference, then we burn a spectral hole followed by another rectangular pulse. We perform this measurement many times and slowly increase the wait-time between the hole burning and the probe pulse. The pulses are sent in at a frequency corresponding to one of the holes. This way we can monitor and fit the decay of the newly created peaks. The result is shown in figure 6.10. On the left are the superimposed plots of the measurements we took (not all performed measurements visible). On the right we show the fitted mean of the steady state amplitude we excited with the second probe pulse, depending on the time between it and the holeburning pulse. From the fit, we obtain the spin diffusion decay constant $T_1^*/2\pi \approx 34.3 \mu\text{s}$, giving us the approximate lifetime of our holes. Furthermore, one can clearly see that the peak height does not decay completely to its previous level. This is evidence of the two kinds of decay mentioned above, however due to the T_1 time in the order of minutes in our diamond, it is not feasible to measure this decay with this method.

6.7 Hahn echos

To further test how much we can manipulate spins in our system, we perform a spin echo measurement, specifically a Hahn echo ([Hahn50]). This works less well in our experiment than in theory, since we cannot perfectly determine what constitutes a perfect $\frac{\pi}{2}$ pulse. Furthermore, only a part of the spins in the system is affected due to the inhomogeneous coupling strengths. By varying the length of π we find the best results at $\pi \approx \frac{1}{2g} \approx 100$ ns. We perform the measurement with our IQ mixing setup and rectangular pulses. To obtain the best results from the echos, we adjust the magnetic field in the [110] direction, where we find the best alignment with the electronic spin axis. This alignment of the magnetic field with the NV axis causes the dipolar field contributions of nearby C^{13} nuclei to cancel each other, reducing a strong source of decoherence(see [Stan12]). With the measurement in figure 6.11, we find the echoes decaying with a spin-spin relaxation time of $T_2 \approx 4.8$ μ s.

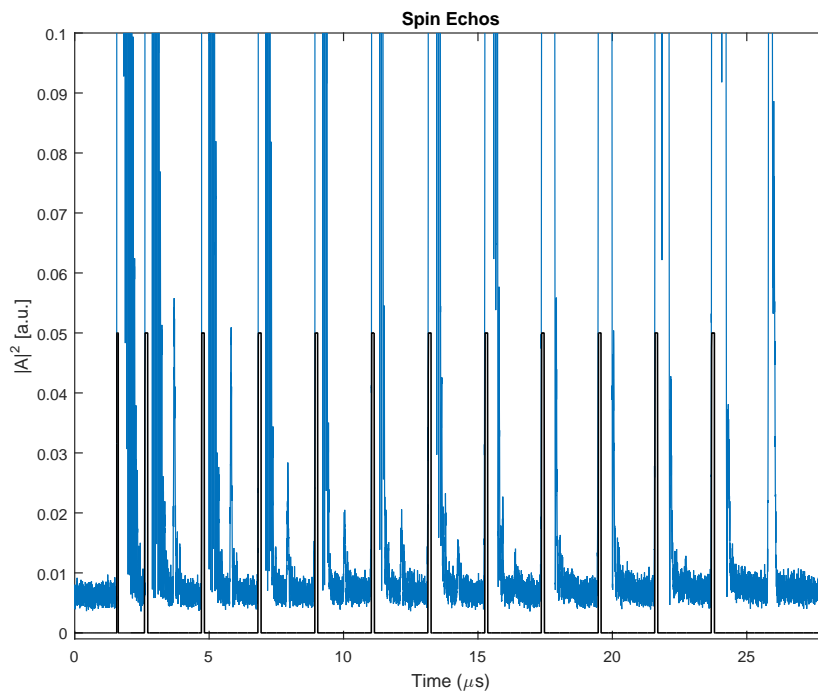


FIGURE 6.11: A Hahn echo measurement, pulse sequence shown in black

6.8 Bistability

The phenomenon of bistability described in chapter 1.5 can occur in quantum optical systems where the coupling between the emitters and the resonator is sufficiently higher than the spin and cavity dissipation rates κ and γ . Our first attempt at measuring bistability proved unseccessful and was performed with the magnetic field aligned in the [110] direction to the NV^- axis, showing no hystereis. In order to significantly increase the coupling strength and thus the cooperativity, we align the field along the [100] axis, increasing the coupling strength g by a factor of $\sqrt{2}$. This allows us to reach a coupling of up to $g = 13.3$ MHz and observe bistability.

We perform the measurement by connecting the setup in our fridge to a VNA. With it, we probe the resonator with a fixed power until we reach a steady state (i.e. the transmission is constant), then slightly increase the power and repeat the process. This way we slowly change our system from the weak driving regime (less spins excited than decaying) to the strong driving regime (more spins excited than decaying), after which we reduce the power again. The measured curve is shown in figure 6.12 and shows a hysteresis with a width of 2 dB m. The data points were created by taking the average of the last 10% of the individual traces to reduce noise. Due to the slow decay times in our system the measurement took about 20 hours to complete. While this makes such measurements a bit tedious, it allows us to observe the decay/excitation dynamics involved, which wouldn't be possible with conventional optical resonators. It is possible to resolve the hysteresis curve further than the 1dB stepsize we used. However, around the transition between weak and strong driving (-32 dB for power increase and -34 dBm for power decrease), this increases the measurement time drastically since the system takes longer and longer to reach a state of equilibrium. It is even technically possible to find a power at which we excite almost exactly the same amount of spins as decay, never really reaching a steady state, though in our case this is not possible due to the limited power resolution of our VNA.

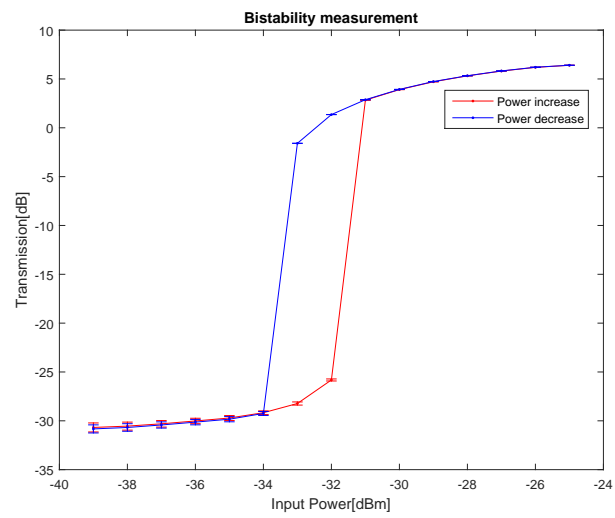


FIGURE 6.12: Hysteresis curve of a bistability measurement

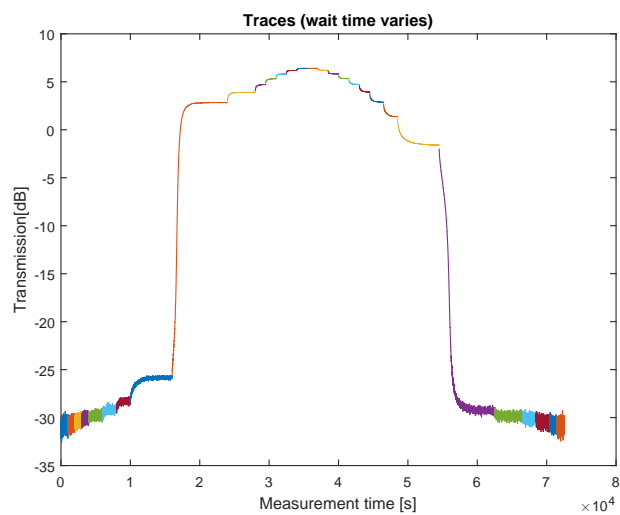


FIGURE 6.13: Individual traces measured with different drive powers

Chapter 7

Conclusion and Outlook

Our main goal was the improvement of our systems dynamics by manufacturing long lived dark states. We clearly achieved this goal in our experiments and showed that within a timeframe of less than $100\ \mu\text{s}$ the coherence properties of our resonator-spin system are strongly increased. This allows us to counteract part of the negative impact inhomogeneous broadening has on our setup.

It may be possible to use this hole-burning technique to create a greater number of holes in the spin ensemble. Such measurements are the subject of ongoing research in our group as of the writing of this thesis, a preliminary result is shown in figure 7.1. Here we burned 4 spectral holes, 2 at each polariton mode, then sent in a sinusoidal excitation pulse. This leads to clear revivals of the pulse, suggesting an oscillation between the newly created peaks in the spectrum. This suggests that the creation of large frequency combs may be possible.

Future applications of spectral hole burning benefit from weak spin diffusion, since this effect mainly determines the timeframe of the improvement. It is also important to consider that such experiments cannot be performed in quick succession; before each measurement the spins must be given time to relax back into the systems equilibrium state. Furthermore, one must make sure that all components operate well when exposed to the high power signals necessary for the hole burning.

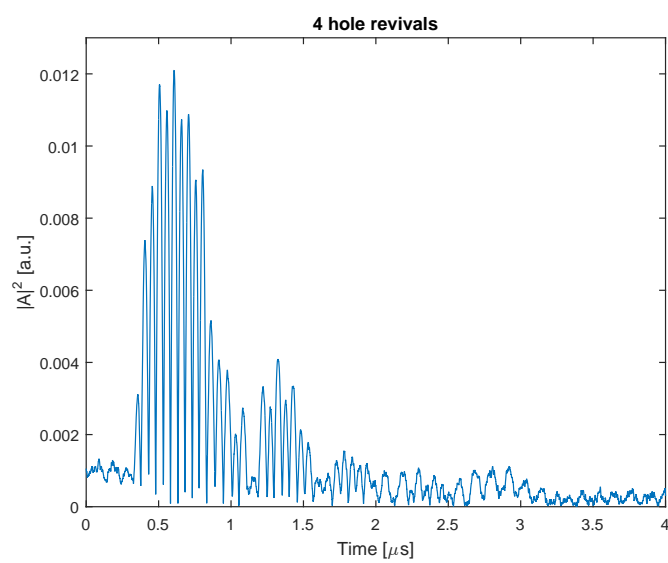


FIGURE 7.1: Revivals visible after sending a sine pulse when 4 holes are present

Appendix A

Frequency analysis of the holes

Here we calculate the form of the holes we create in the frequency spectrum. This form can be derived by taking the Fourier transform of the signal we modulate onto the carrier. In the case of a Gaussian form, the result would also be Gaussian, but since we switch off the signal at its maximum, it gets a bit more complicated: We have to calculate the Fourier transform of half a Gaussian. To do this, we start with the Fourier transform of a Gaussian and split the exponential into its sine and cosine parts. The fact that we only use half a Gaussian is incorporated through the borders of the integral.

$$F \left[e^{-\frac{t^2}{a^2}} \right] (\omega) = \frac{1}{\sqrt{2\pi}} \int_0^\infty e^{-\frac{t^2}{a^2}} e^{i\omega t} dt \quad (\text{A.1})$$

$$= \frac{1}{\sqrt{2\pi}} \left[\int_0^\infty e^{-\frac{t^2}{a^2}} \cos(\omega t) dt - i \int_0^\infty e^{-\frac{t^2}{a^2}} \sin(\omega t) dt \right] \quad (\text{A.2})$$

We calculate these integrals with Abramowitz and Stegun (1972, p. 302, equations 7.4.6, 7.4.7); the integral at the end of equation A.3 is known as the imaginary error function, which can only be solved numerically.

$$= \frac{a}{\sqrt{8}} e^{-\omega^2 a^2/4} - \frac{a}{\sqrt{2\pi}} i e^{-\omega^2 a^2/4} \int_0^{\frac{\omega a}{2}} e^{t^2} dt \quad (\text{A.3})$$

$$= \frac{a}{\sqrt{8}} e^{-\omega^2 a^2/4} \left[1 - i \cdot \operatorname{erfi} \left(\frac{\omega a}{2} \right) \right] \quad (\text{A.4})$$

This function is imaginary, the real form of our holes is given by its absolute value: a Gaussian function modified by the erfi function. To classify the width of the holes, we use the FWHM. To obtain it, we normalize the absolute value of the Fourier transform to 1 (eliminating the prefactors) and set it equal to $\frac{1}{2}$

$$|F(\omega)| = \left| e^{-\omega^2 a^2/4} \left[1 - i \cdot \operatorname{erfi} \left(\frac{\omega a}{2} \right) \right] \right| = \frac{1}{2} \quad (\text{A.5})$$

Substituting ω with $2\pi f$ results in:

$$|F(f)| = \left| e^{-f^2 a^2 \pi^2} [1 - i * \operatorname{erfi}(\pi f a)] \right| = \frac{1}{2} \quad (\text{A.6})$$

In our experiment, $a = \frac{1}{500e3} \mu\text{s}$ and solving this equation numerically gives us a FWHM of 473 kHz. The exact Gauss-like form of the holes is shown in figure A.1.

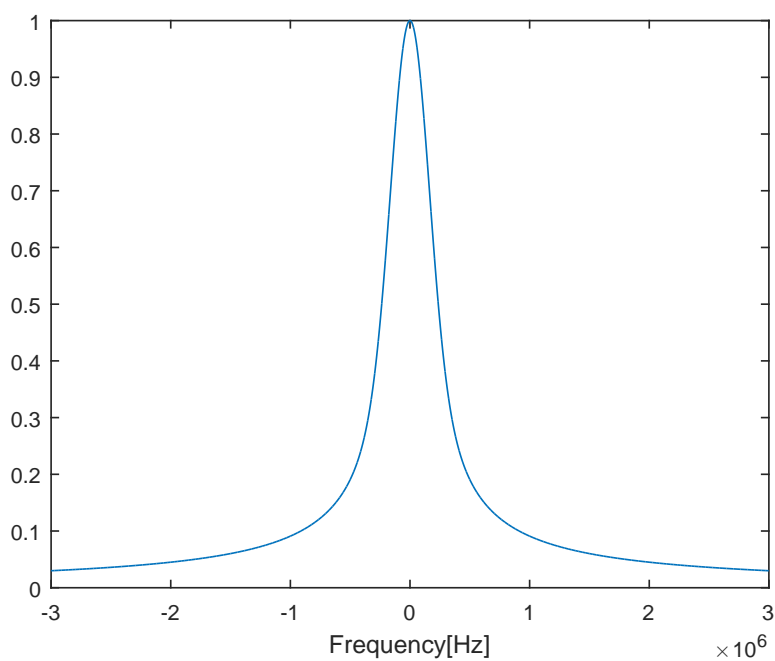


FIGURE A.1: The modified Gaussian that defines the shape of the spectral hole

Acknowledgements

For their patience and continuous support I want to thank my family and friends. For their competent help and guidance, as well as answering so many of my questions, I want to thank my thesis advisors Johannes Majer, Stefan Putz and Andreas Angerer, as well as my colleagues Thomas Astner and Stefan Nevlacsil.

Bibliography

- [Ams13] Robert Amsüss. *Strong coupling of an NV^- spin ensemble to a superconducting resonator*. Doctors thesis 2013
- [Ch97] E. Chen and S. Chou. Characteristics of coplanar transmission lines on multilayer substrates: Modeling and experiments *Microwave Theory and Techniques, IEEE Transactions on* 45, 6 (1997), 939-945.
- [Dicke54] R.H.Dicke. *Coherence in Spontaneous Radiation Processes*. *Physical Review* Volume 93, Number 1 (1954)
- [Diniz11] I. Diniz, S.Portolan, R.Ferreira, J.M. Gerard, P.Bertet, and A.Auffeves *Strongly coupling a cavity to inhomogeneous ensembles of emitters: Potential for long-lived solid-state quantum memories* *Phys. Rev. A* 84, 063810 (2011)
- [Doh13] Marcus W. Doherty, Neil B. Manson, Paul Delaney, Fedor Jelezko, Jörg Wrachtrup and Lloyd C.L. Hollenberg. *The nitrogen-vacancy colour centre in diamond* arXiv:1302.3288
- [Fano61] U.Fano. *Effects of Configuration Interaction on Intensities and Phase Shifts*. *Physical Review* Volume 124, Number 6 (1961)
- [Hahn50] E.L.Hahn. *Spin Echoes* *Phys. rev.* 80, 580
- [Har06] J. Harrison, M.J. Sellars, N.B. Manson *Measurement of the optically induced spin polarization of N-V centres in diamond* *Diamond and Related Materials* 15 (2006) 586-588
- [Hol39] H.Primakoff, T.Holstein *Many-Body Interactions in Atomic and Nuclear Systems* *Phys. Rev* Vol 55 (1939)
- [Kol12] Christian Koller. *Towards the experimental realization of Hybrid Quantum Systems*. Doctors thesis 2012

- [Krim15] Dmitry O. Krimer, Benedikt Hartl, and Stefan Rotter. *Hybrid Quantum Systems with Collectively Coupled Spin States: Suppression of Decoherence through Spectral Hole Burning*. Phys. Rev. Lett. 115, 033601 (2015)
- [Kur11] Z.Kurucz, J.H.Wesenberg, and K.Mölmner *Spectroscopic properties of inhomogeneously broadened spin ensembles in a cavity* Phys. Rev A 83, 053852 (2011)
- [Lev09] Malcolm H.Levitt *Spin dynamics* ISBN 978-0-470-51117-6 (2009)
- [Lou74] Lounasmaa, O.V. *Experimental Principles and Methods Below 1 K* London: Academic Press. p. 316. ISBN 978-0124559509 (1974)
- [Mart11] M. J. Martin, D. Meiser, J. W. Thomsen, Jun Ye, and M. J. Holland. *Extreme nonlinear response of ultranarrow optical transitions in cavity QED for laser stabilization*. Physical Review A 84, 063813 (2011)
- [Nob13] T. Nöbauer, K. Buczak, A. Angerer, S. Putz, G. Steinhauser, J. Akbarzadeh, H. Peterlik, J. Majer, J. Schmiedmayer, and M. Trupke. *Creation of ensembles of nitrogen-vacancy centers in diamond by neutron and electron irradiation* arXiv:1309.0453
- [Pob07] F Pobell. *Matter and methods at low temperatures*, F Pobell (2007)
- [Purc46] *Proceedings of the American Physical Society* Phys. Rev. 69, 674 (1946)
- [Putz14] S. Putz, D. O. Krimer, R. Amsüss, A. Valookaran, T. Nöbauer, J. Schmiedmayer, S. Rotter and J. Majer. *Protecting a spin ensemble against decoherence in the strong-coupling regime of cavity QED*. Nature Physics Letters DOI:10.1038/NPHYS3050 (2014)
- [Putz15] S. Putz, A. Angerer, D. O. Krimer, R. Glattauer, William J. Munro, S. Rotter, J. Schmiedmayer and J. Majer. *Engineering Long-Lived Dark-States in Electron Spin Ensembles* arXiv:1512.00248
- [Rabi37] I.I.Rabi *Space quantization in a gyrating magnetic field* Phys. Rev 51 (1937)
- [SG08] R. J. Schoelkopf and S. M. Girvin. *Wiring up quantum systems*. Nature Vol 451/7 (2008)
- [Stan12] P. L. Stanwix, L. M. Pham, J. R. Maze, D. Le Sage, T. K. Yeung, P. Cappellaro, P. R. Hemmer, A. Yacoby, M. D. Lukin, and R. L. Walsworth *Coherence of nitrogen-vacancy electronic spin ensembles in diamond*. Physical Review B 82, 201201(R)(2010)
- [TC68] M. Tavis and F. W. Cummings. *Exact Solution for an N-Molecule-Radiation-Field Hamiltonian* Phys. Rev. 170, 379-384 (1968)